An experimental study of rime ice accretion on bundled conductors

Ramsankar Veerakumar, Haiyang Hu, Linchuan Tian, Nianhong Han, Hui Hu [*]

Dept. of Aerospace Engineering, Iowa State University, Ames, IA 50011, USA

ABSTRACT

The dynamic ice accretion process on bundled electrical power conductors and icing-induced effects on the aerodynamic forces acting on the conductors were examined experimentally. An Icing Research Tunnel was used to generate a typical atmospheric rime icing condition experienced by power transmission cables. Two pieces of Aluminum-Conductor-Steel-Reinforced (ACSR) cables were mounted in the icing wind tunnel with different spacing and angular displacements with respect to the incoming airflow. While ice accretion was found to take place primarily on the frontal surfaces of the bundled conductors, the accreted ice layers resembled well the twisted outer strands of the ACSR conductors. Averaged outer profiles of the iced conductors were elliptical with the semi-minor axis being the radius of the conductors and the semi-major axis passing through the foremost frontal points of the accreted ice layers. The icing process on the windward conductor was almost unaffected by the existence of the leeward conductor. The ice accretion and resultant aerodynamic force acting on the leeward conductor were found to vary significantly, depending on the spacing and angular displacements between the bundled conductors. The windward conductor was found to induce a "shadowing effect" by intercepting airborne supercooled water droplets to prevent them from impinging onto the leeward conductor, resulting in much less ice accretion and smaller aerodynamic drag acting on the leeward conductor. The aerodynamic force measurements were correlated with the acquired ice accretion images and wake flow field around the bundled conductors to elucidate the underlying physics.

1. Introduction

Snowing and icing in winter is one of the most serious natural disasters faced by electrical power transmission networks [1–4]. Ice accretion on the electric power conductors due to accumulation of snow, freezing rain, and airborne supercooled water droplets is reported to cause significant reliability degradation to power distribution networks during cold winters. Catastrophic incidents/accidents were found to occur in the past years due to severe ice accretion on electric power conductors. An icing event in the winter of 1998 in Quebec and Ontario, Canada, was found to destroy hundreds of miles of power transmission cables, leading to a major power outage for about one million customers for up to 30 days [5]. At the same time, the direct material cost to reconstruct the destroyed power conductors was estimated to be billions of Canadian dollars, with the associated social cost exceeding three times more [5]. Another extremely severe icing disaster occurred in the spring of 2008 in southern China, which caused massive damage to the power grids in 13 provinces, resulting in a weeks-long blackout that affected over 20 million people [6,7].

It is well known that ice accretion on a surface can be either *rime*, *glaze,* or *mixed* icing, depending on icing conditions such as ambient temperature, liquid water content (LWC), wind speed, and sizes of airborne water droplets. Relatively low LWC and cold temperatures (e. g., less than −10 °C) would favor a *rime icing* process where almost all the airborne droplets would be frozen into ice immediately upon impinging onto the structural surfaces [8]. However, warmer temperatures (e.g., > −5 °C) and higher LWC levels in the incoming airflow would usually cause a wet icing regime where only a portion of the impinged droplets would be frozen into solid ice instantly in the impingement area, while the remaining unfrozen water would run back over and then freeze into ice subsequently, causing *glaze ice* formation [9] *Mixed icing* refers to a situation with a simultaneous appearance or a combination of the rime and glaze ice characteristics [10].

An improved understanding of the icing process on electrical power conductors and the resultant effects on the aerodynamic forces acting on the iced conductors is essential for developing effective and robust measures for icing mitigation. While extensive investigations have been conducted in recent years to examine the dynamic ice accretion process

on power conductors and the resultant aerodynamic load changes induced by the ice accretion [3,6,7,9,11–16], most of those investigations were performed with simplified cylindrical test models with smooth surfaces. However, Aluminum-Conductor-Steel-Reinforced (i.e., ACSR) cables are the most used primary and secondary distribution conductors in reality because of their economy, dependability, and strength-to-weight ratio. It was reported recently that the rough, twisted outer strands wrapping around the ACSR conductors would significantly affect the characteristics of ice accretion and resultant aerodynamic forces [17]. It should also be noted that while most previous studies were focused on individual conductors, bundled conductors are nowadays widely used in high-voltage power transmission [11,18,19] For example, 2-bundled conductors are usually used for power transmission of 220 kV, 4-bundled conductors for 500 kV, 6-bundled conductors for 750 kV, and even 8-bundled conductors are widely utilized for ultra-high voltage power transmission of 1,000 kV [19]. Due to the presence of the windward conductors in a bundled configuration, the ice accretion characteristics are significantly different from those of a single conductor [14,15,18]. While the ice accretion on a windward conductor is the same as that on a single conductor, the leeward conductor was found to have a smaller droplet impacting velocity, lower local collision efficiency and less accreted ice mass than those of the windward conductor. The growth and the shape of the ice layer accreted on the leeward conductor were found to vary substantially as a function of the distance between the conductors. Substantial errors were found when the icing model based on the findings of individual conductors was used to predict the icing characteristics on bundle conductors [14,20].

Several investigations were performed to examine ice accretion on bundled conductors. He et al. [18] conducted numerical and experimental studies to investigate the rime icing process on bundled cylindrical conductors. They found that the icing characteristics on the windward conductor are almost the same as those of a single conductor (i.e., It has the same droplet collision efficiency and accreted ice mass), suggesting that the leeward conductor would not affect the icing characteristics of the windward conductor. However, the icing characteristics of the leeward conductors were found to vary greatly, i.e., having a smaller droplet impacting velocity, lower local collision efficiency and less accreted ice mass. Li et al. [11] reported an experimental study to examine the aerodynamic performance of 4-bundle conductors with artificial ice structures on the conductor models. They found that the windward conductor's existence would affect the leeward conductor's aerodynamic performance substantially until the angular displacement between the conductors is greater than 10° in respective to the incoming airflow. Xue et al. [21] and Liang et al. [22]conducted comparative studies with different shapes of artificial ice structures (e.g., crescent-shaped vs. cylinder-sector-shaped artificial ice layers) attached to bundled conductors. They found that the aerodynamic characteristics of the bundled conductors with crescent-shaped ice structures significantly differed from those of the iced conductors with cylinder-sector-shaped ice structures. It suggests that the actual shapes of the ice layers accreted on the conductors would affect their aerodynamic characteristics greatly. The research findings highlight the importance of conducting ice accretion experiments to generate realistic ice shapes instead of using approximated artificial ice shapes to improve our understanding of the characteristics of ice accretion and resultant aerodynamic forces acting on bundled conductors.

In the present study, a comprehensive experimental campaign is conducted to examine the characteristics of dynamic rime ice accretion on high-voltage power conductors in a bundled configuration and to quantify the variations of the aerodynamic forces acting on the bundled conductors induced by the ice accretion. A typical atmospheric rime icing condition experienced by power conductors was generated using an Icing Research Tunnel available at Iowa State University (i.e., ISU-IRT). Two ACSR power cables/conductors were mounted in ISU-IRT with different spacing and angular displacements respective to the incoming airflow. While a high-speed imaging system was used to record

the dynamic icing process, a novel 3D profile scanning system was also utilized to measure the 3D shapes of the iced ACSR conductors under different test conditions. In addition to measuring the dynamic aerodynamic drag forces acting on the bundled conductors using high-sensitive force/moment transducers, the wake flows behind the bundled conductors were also characterized with a Particle Image Velocimetry (PIV) system. The PIV flow field measurements were correlated with the aerodynamic force measurements and the acquired ice accretion images to gain further insight and improve our understanding of the ice accretion over bundled conductors (see Fig. 1).

2. Experimental setup and measurement systems

2.1. Brief introduction of the experimental setup

A multi-function Icing Research Tunnel of Iowa State University (i.e., ISU-IRT in short) was used to conduct the ice accretion experiments. The tunnel has a transparent test section of 400 mm in width × 400 mm in height × 2.00 m in length. It can generate a recirculating airflow with the airflow temperature down to −25 °C and speed up to 60 m/s in the test section. An array of 8 pneumatic spray atomizers (IKEUCHI BIMV 8002) was installed in the ISU-IRT to inject micro-sized water droplets (i.e., 10 ∼ 100 μm in size) into the airflow. The droplet size and the liquid water content (LWC) level inside ISU-IRT can be adjusted by changing the air/water pressure, and the water flow rate supplied to the spray atomizers. ISU-IRT has been used to simulate various atmospheric icing phenomena for various engineering applications, including aircraft/aero-engine icing [8,23–26], bridge cable anti-/de-icing [27–29], and wind turbine icing mitigation [30–33].

The bundled conductor models used in the present study comprise two pieces of typical ACSR power conductors. While the ACSR conductors have an outer diameter of $D = 29$ mm with sixteen twisted aluminum outer strands (the diameter of each strand being 4.7 mm) wrapping around the cable surface, its spanwise length was set to be the same as the test section width (i.e., 400 mm). The surfaces of the ACSR conductors were found to be hydrophilic, with the contact angle of sessile water droplets on the surfaces being ∼ 65°, which agrees well with the value given by Li et al. [34].

As shown schematically in Fig. 2, the bundled conductors were mounted in the test section in tandem. While the spacing between the ACSR models (i.e., the value of L) was changed from 6D to 14D, the angular displacement (i.e., the value of $θ$) with respective to the incoming airflow was also varied from 0° to 15° for different test cases. It should also be noted that, similar to the finding reported by He et al. [18], the ice accretion process on the windward conductor was almost unaffected by the leeward conductor. Thus, icing characteristics on the windward conductor were almost identical to those on a single conductor (i.e., having the same droplet collision efficiency and accreted ice mass) given in Veerakumar et al. [17]. Therefore, while the icing characteristics of the windward conductor are used as the comparison baseline, the present study will focus primarily on the leeward conductor to elucidate the interferences between the bundled conductors with different configurations.

During the experiments, the velocity of the incoming airflow in the test section of ISU-IRT was kept at $V_∞ = 20$ m/s (i.e., a typical wind speed experienced by power cables in icing events) with the corresponding Reynolds number of the conductor model being $Re_D ≈ 50,000$ (i.e., with the air density and viscosity at $T_∞ = −15$ °C used in the present study). It is well known that the ice accretion process over a solid surface could be of several types depending on the combined effects of wind speed, Liquid Water Content (LWC) level, ambient temperature, and size of the super-cooled water droplets [35]. Following up on the recent work of Veerakumar et al. [17], a typical rime icing condition was generated in ISU-IRT with $LWC = 1.0$ g/m³ and $T_∞ = −15.0$ °C. The turbulence level of the incoming airflow in ISU-IRT is measured to about 1.0%. The rime icing experiments for all the test cases were designed to
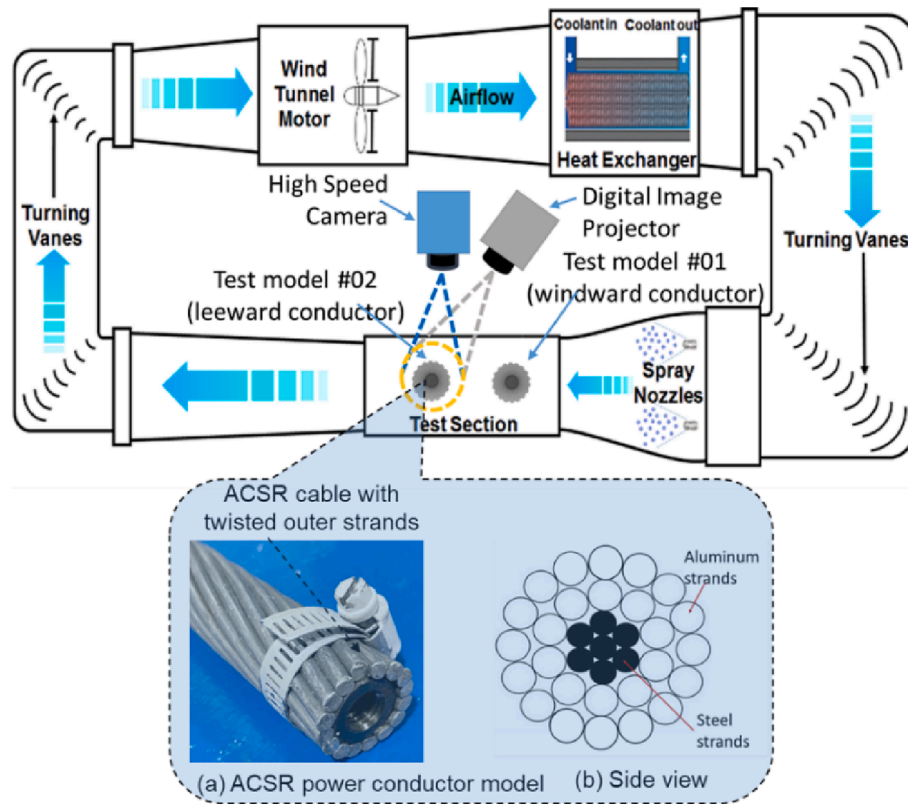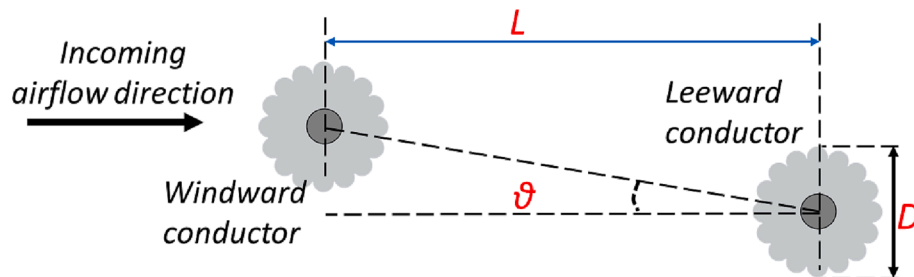
Fig. 1. Experimental setup used in the present study.

Fig. 2. The layout of the bundled conductors used for the present study.

have the same duration of 600 s.

2.2. Characterization of the ice accretion on the bundled conductors

A high-speed imaging system (i.e., PCO-Dimax-S1 camera with 1008 pixels by 1008 pixels in spatial resolution and acquisition rate up to 25,000 Hz) mounted with a Nikkor 2.8D optical lens was used to take snapshot images of the dynamic icing process on the leeward conductor. Low-flicker illumination for the image acquisition was provided by a pair of 150 W fiber-coupled halogen lamps (AmScope, HL250-AS).

A three-dimensional (3D) profile scanning system was also used to measure the 3D shapes of the iced bundled conductors. While the 3D profile scanning system is based on a structured light triangulation principle [36], more details of the technical basis and measurement procedure for the 3D shape measurements can be found in our recent papers [17,28,29,37].

The 3D shape measurements of the iced conductors are set to be around the midspan of the bundled conductors with a field view of 100 mm by 100 mm. The measurement accuracy of the 3D profile scanning system was estimated by measuring 3D printed hemispherical roughness elements on a test plate with nominal diameters changing from 1.0 mm to 8.0 mm. Based on the measurements of 500 points around the hemispherical roughness elements, the measurement uncertainty was estimated to be about 2.0% [9].

2.3. Measuring aerodynamic forces acting on the bundled conductors.

The aerodynamic forces acting on the bundled conductors during the ice accretion process were measured using high-sensitive force transducers (ATI-IA Mini 45) mounted at two ends of the conductors. While the force/moment transducers can measure aerodynamic forces acting on the bundled conductors along all three orthogonal axes, only the aerodynamic drag data were presented and analyzed in the present study for conciseness. The precision of the force-moment transducer for the force measurements is $\pm$ 0.25% of the full range. During the experiments, the force/torque transducers were synchronized via a 16-bit data acquisition system (NI USB-6218) at the data acquisition rate of 1,000 Hz.

2.4. Wake measurements behind the bundled conductors

The wake characteristics behind the bundled conductors were quantified using a Particle Image Velocimetry (PIV) system. The micro-sized, airborne water droplets inside ISU-IRT were used as the tracer particles for the PIV measurements. Since the airborne water droplets were measured to be $\sim 20~\mu m$ in MVD, the corresponding Stokes number of the droplets was estimated to be about 1.0 (i.e., $St = \frac{\rho_p d_p^2 U}{18 \mu D} \approx 1.0$ [38], suggesting that the airborne water droplets would follow the airflow well. A double-pulsed Nd: YAG laser (Evergreen, Big Sky Laser, 200 mJ/pulse @ 532 nm) and a set of optics were used to generate a thin laser sheet (~1.0 mm in thickness) to illuminate the flow field. A high-resolution 12-bit digital camera (2048-pixel by 2048-pixel resolution, PCO-Tech) with a Nikon Nikkor lens was used to acquire images of the tracer particles. A Digital Delay Generator (Berkeley Nucleonics, Model 565) was used to control the timing of the image acquisition and laser illumination. For the PIV measurements of the present study, while the measurement window size was set to be 200 mm by 200 mm, the instantaneous PIV image pairs were acquired at a frame rate of 15 Hz.

Commercial software of LaVison^{TM} - Davis 7.2 was used for the PIV image process. The size of the interrogation windows for the PIV image processing was 32 pixels × 32 pixels with a 50% effective overlap rate. As a result, the PIV measurement results were found to have a spatial resolution of 1.5 mm × 1.5 mm and an estimated measurement uncertainty of $\sim 2.0~\%$.

3. Experimental results and discussions

3.1. Effect of the spacing between the bundled conductors

As aforementioned, a high-speed imaging system was used to record the dynamic ice accretion on the surfaces of the ACSR conductors. Fig. 3 shows representative images taken after undergoing 600 s of the ice accretion process under the test conditions of $V_\infty = 20$ m/s, $T_\infty = -15\,^\circ$C, and $LWC = 1.0$ g/m^3, which reveal the global features of the ice accretion on the leeward conductor as a function of the spacing between the bundled conductors. For the experiments to evaluate the effects of the spacing between the bundled conductors, the windward and leeward conductors were aligned along the incoming airflow direction with the angular displacement of bundled conductors being zero (i.e., $\theta = 0^\circ$).

With the ambient temperature being well below the water freezing temperature (i.e., $T_\infty = -15\,^\circ$C), since the latent heat of fusion released during the phase change (i.e., solidification) process would be dissipated rapidly [8], the supercooled water droplets were found to freeze into ice instantly upon impinging onto the conductor surfaces. While ice accretion was found to take place primarily over the frontal surfaces of the ACSR conductors (i.e., within the direct impinging zone of the airborne droplets), no water runback was observed on the conductor surfaces. The accreted ice structures were grainy and opaque with a milky-white appearance. The experimental observations confirmed that the ice accretion on the bundled conductors is a rime icing process [8,39]. Similar to that reported by He et al. [18], the presence of a leeward conductor would not affect the icing process of the windward conductor.

A comprehensive image processing procedure [40,41] was used in the present study to extract quantitative information (e.g., the thickness of the accreted ice layer near the leading edge of the ACSR conductors) from the acquired ice accretion images. Fig. 4 gives the results extracted from the acquired ice accretion images to reveal the variation of the averaged thickness of the ice layers accreted near the leading edge of the bundled conductors (i.e., spatially averaged along the spanwise direction of the ACSR conductors within the measurement window given in Fig. 3) as a function of the ice accretion time for some selected test cases.

As revealed in Fig. 4, the rime ice layers accreted on the bundled conductors grew linearly with the increasing ice accretion time, as expected. Even though the bundled conductors were exposed to the same rime icing conditions, the accreted ice layer on the leeward conductor was much thinner than on the windward conductor. With the increasing spacing between the bundled conductors, the ice layer on the leeward conductor was found to increase gradually. More specially, after undergoing 600 s of the rime icing experiment, while the averaged ice
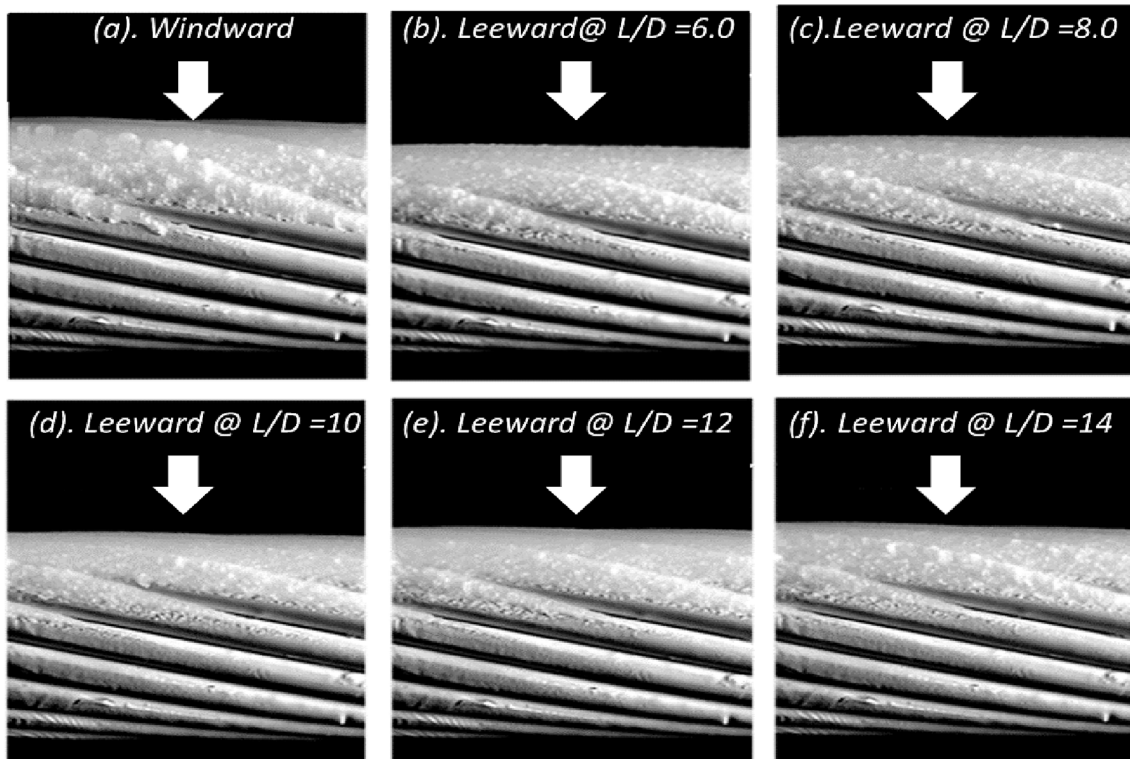

Fig. 3. Acquired ice accretion images after undergoing 600 s of the rime ice accretion for the test cases with different spacing between the bundled conductors.
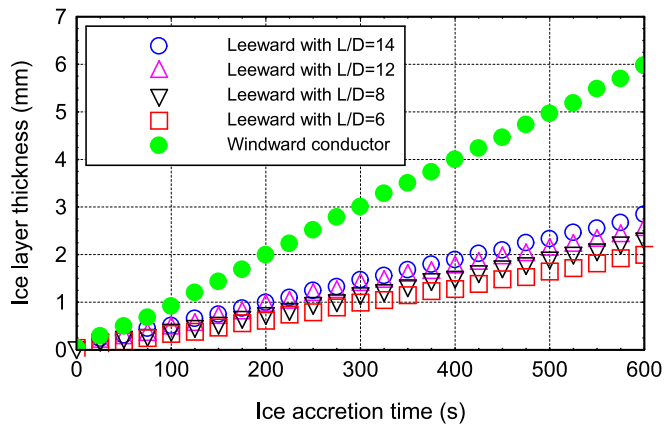
Fig. 4. Time evolution of the accreted ice thickness at the different spacing between the bundled conductors.

thickness near the leading edge of the windward conductor was measured to be 5.98 mm (i.e., the corresponding growth rate of the ice layer thickness being ~ 0.010 mm/s), the corresponding value on the leeward conductor was found to become only 2.01 mm for the test case with L/D = 6 (i.e., the growth rate of the ice layer thickness being 0.0034 mm/s). The corresponding value was found to increase to 2.69 mm as the spacing between the bundled conductors was increased to L/D = 14 (i.e., the growth rate of the ice layer thickness being ~ 0.0045 mm/s), which is about 34% increase than the test case with L/D = 6, but still much thicker than that on the windward conductor (i.e., becoming ~ 45% of that on the windward conductor). The experimental findings can be explained by the fact that, since the leeward conductor would be in the wake of the windward conductor from the perspective of the incoming airflow, the windward conductor would intercept a great portion of the airborne supercooled water droplets and prevent them from impinging onto the leeward conductor (i.e., windward conductor induces a "shadowing effect"). With the spacing between the bundled conductors being L/D = 6.0, as shown in Fig. 3b, the windward conductor's strong "shadowing effect" resulted in a much thinner ice layer accreted on the leeward conductor (i.e., only 34% of that on the windward conductor). With the increasing spacing between the bundled

conductors, the "shadowing effect" of the windward conductor would become less severe. As a result, more airborne supercooled water droplets could impinge onto the leeward conductor, causing a thicker ice layer accreted on the leeward conductor (i.e., increasing to 45% of that on the windward conductor for the L/D = 14 case).

In the present study, as mentioned earlier, a DIP-based 3D profile scanning system was also used to quantify the 3D shapes of the ice layers accreted on the conductors. Fig. 5 to Fig. 7 show the measurement results obtained after 600 s of the rime icing experiments for three selected test cases, i.e., the iced windward and leeward conductors with L/D = 6 and 12, respectively. Based on the measured 3D profile of the iced conductors, while the profiles of the accreted ice layers at any cross sections can be extracted quantitatively, averaged profiles of the accreted ice layers can also be determined by averaging the measured ice layer profiles in ~ 20 cross-sections along the spanwise direction of iced conductors. The characteristics of the icing process on the bundled conductors were revealed more clearly and quantitatively from the measured 3D shapes of the iced conductors.

As shown clearly in Fig. 5, since the droplets would be frozen into solid ice instantly upon impacting the windward conductor, ice structures were found to accrete primarily over the frontal surface of the conductor (i.e., within the direct impinging zone of the airborne droplets). Corresponding to the higher water droplet collection efficiency near the conductor leading edge [35], the ice accretion near the conductor leading edge was much thicker than those at downstream locations. As revealed clearly from the measurement results given in Fig. 5(b) and 5(c), while the accreted rime ice layer was found to resemble well the twisted outer strands of the ACSR conductor, the averaged profile of the ice layer accreted over the frontal conductor surface is elliptical (i.e., with the semi-minor axis being the radius of the ACSR conductor and the semi-major axis passing through the foremost front point of the ice layer accreted on the conductor). It indicates that, because of the ice accretion on the frontal surface, the outer profile of the iced conductor would be changing gradually from a bluff body to being more streamlined in the cross-section. Therefore, the aerodynamic drag of the iced ACSR conductor would decrease gradually due to the formation of the more streamlined frontal profile, which was confirmed by the measured aerodynamic force data to be presented later. It should also be noted that, based on the 3D profile scanning result of the iced conductor given in Fig. 5, the averaged ice thickness near the conductor
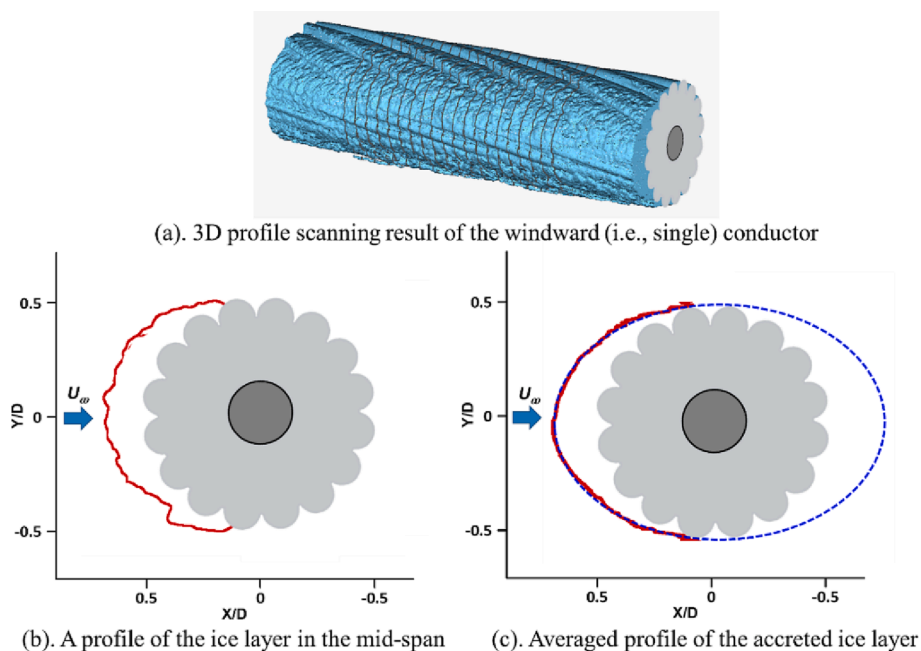

(a). 3D profile scanning result of the windward (i.e., single) conductor

(b). A profile of the ice layer in the mid-span

(c). Averaged profile of the accreted ice layer

Fig. 5. 3D profile scanning results of the iced windward conductor.

leading edge was measured to be 5.91 mm after undergoing 600 s of the rime icing experiment, which agree well with the value measured independently and presented in Fig. 4.

Fig. 6 gives the measured 3D shape of the iced leeward conductor with L/D = 6.0. As aforementioned, since a portion of the supercooled water droplets carried by the incoming airflow would be intercepted by the windward conductor, fewer airborne droplets would be able to impinge onto the leeward conductor due to the "shadowing effect" of the windward conductor. As a result, a much thinner ice layer was found to accrete on the frontal surface of the leeward conductor compared to that of the windward conductor. As revealed clearly from the measurement result given in Fig. 6(b), the accreted rime ice layer resembled well the twisted outer strands of the ACSR conductor, causing the generation of well-organized ice humps over the conductor surface. While the averaged profile of the ice layer accreted over the frontal surface of the leeward conductor was still found to be elliptical, the semi-major axis of the ellipse was found to become much shorter than that of the windward conductor case due to the much thinner ice layer accreted over the frontal surface of the leeward conductor. Based on the measurement result given in Fig. 6(c), the ice thickness near the leading edge of the leeward conductor was found to be about 2.2 mm for the test case with L/D = 6.0, which agrees well again with the measured value reported in Fig. 4 (i.e., the differences being within ~ 4%).

As the bundle spacing increased to L/D = 12, since the wake flow of the windward conductor had a longer distance to recover, more airborne droplets were entrained into the wake flow, causing more ice to accrete on the leeward conductor. As revealed from the measured 3D shape of the iced leeward conductor given in Fig. 7, the ice thickness near the conductor's leading edge became 2.76 mm, which is about 35% more than that of the L/D = 6.0 case. However, the accreted ice layer on the leeward conductor was still much thinner (i.e., ~54% thinner) than on the windward conductor. It suggests that even for the test case with the bundle spacing increased to 12D, the "shadowing effect" from the windward conductor was still substantial, causing the much thinner ice layer on the leeward conductor.

With the 3D profile scanning results given in Fig. 5 to Fig. 7, the total volume of the ice layers accreted on the ACSR conductors can also be determined quantitatively. According to Liu et al. [42], typical rime ice would have a density of ~ 880 kg/m^3. Hence, the total mass of the ice

structures accumulated on the bundled conductor models can also be estimated quantitatively. After undergoing 600 s of rime ice accretion, while the total ice mass accreted on the windward conductor per unit length was estimated to be 0.12 Kg/m, the values for the leeward conductor were found to become 0.042 Kg/m and 0.055 Kg/m for the test cases with the spacing between the bundled conductors being L/D = 6.0 and L/D = 12, respectively.

The present study also measured the aerodynamic forces acting on the bundled conductors during the ice accretion process with high-sensitivity force/moment transducers. While the duration of the aerodynamic force measurements was set to be 700 s for each experiment, the water spray system of ISU-IRT was switched on (i.e., to start the rime ice accretion process) at 100 s after switching on the force transducers. By averaging the instantaneous aerodynamic force data before starting the icing experiment, the averaged aerodynamic drag of the "clean" windward conductor, D_0, was determined, which is used as the comparison baseline in the present study. It is worth noting that the measured aerodynamic drag coefficient of the "clean" windward conductor was C_D = 1.05, which agrees well with the numerical simulation result reported by Qi et al.[43].

Fig. 8 shows the aerodynamic drag data during the icing experiments. The measured aerodynamic drag data were represented in term of D/D_0, i.e., normalized by the baseline value of D_0, which is the aerodynamic drag of the "clean" windward conductor. While instantaneous aerodynamic force data were acquired at a data acquisition frequency of 2,000 Hz, only the moving averaged values (i.e., averaging the instantaneous force measurements every 5 s) are presented here for comparison.

It was shown clearly in Fig. 8 that the windward conductor had a distinctly greater aerodynamic drag than those acting on the leeward conductors. As described above, the ice accretion over the frontal conductor surfaces would cause the outer profiles of the iced conductors to change gradually from bluff bodies to becoming more streamlined in the cross-section, thereby, smaller aerodynamic drag forces acting on the iced conductors. Therefore, the aerodynamic drag experienced by the windward conductor was reduced to ~ 93% of the "clean" conductor after undergoing 600 s of rime ice accretion.

Due to the "shadowing effect" from the windward conductor, while the aerodynamic drag acting on the leeward conductor became much
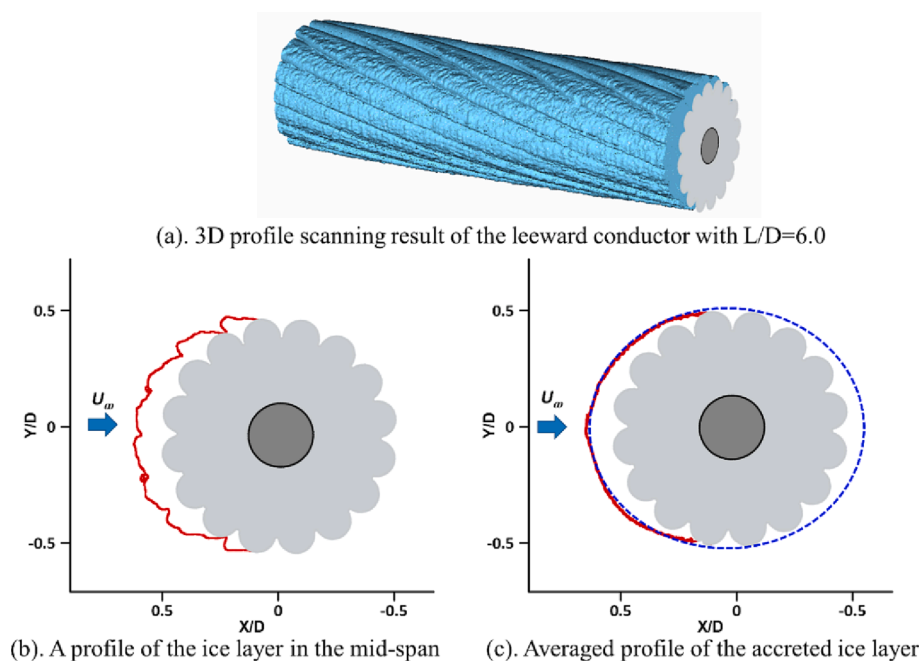

(a). 3D profile scanning result of the leeward conductor with L/D=6.0

(b). A profile of the ice layer in the mid-span

(c). Averaged profile of the accreted ice layer

Fig. 6. 3D profile scanning results of the iced leeward conductor for the test case with L/D = 6.0.

(a). 3D profile scanning result of the leeward conductor with L/D=12

(b). A profile of the ice layer in the mid-span

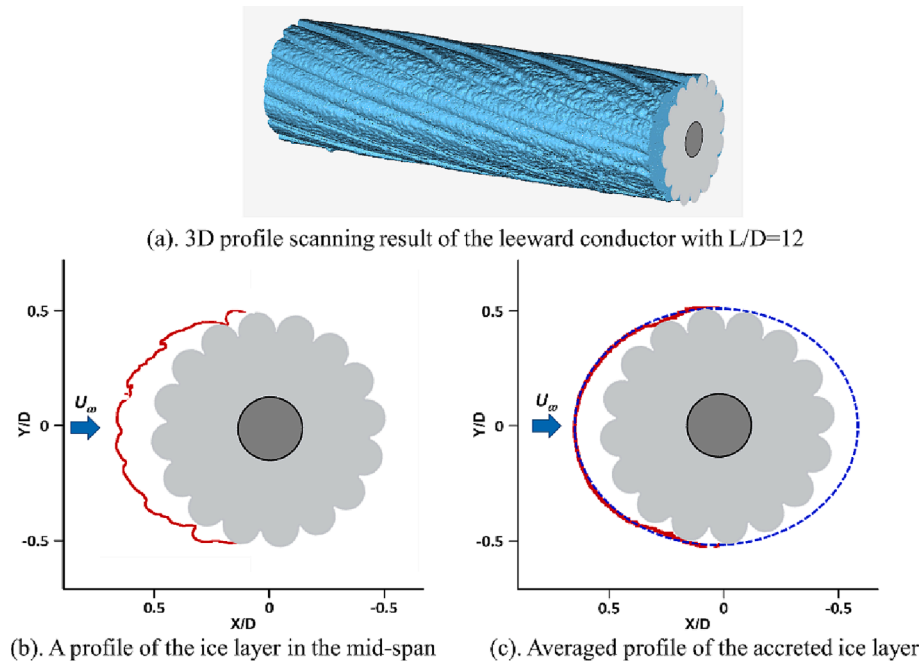(c). Averaged profile of the accreted ice layer

Fig. 7. 3D profile scanning results of the iced leeward conductor for the test case with L/D = 12.
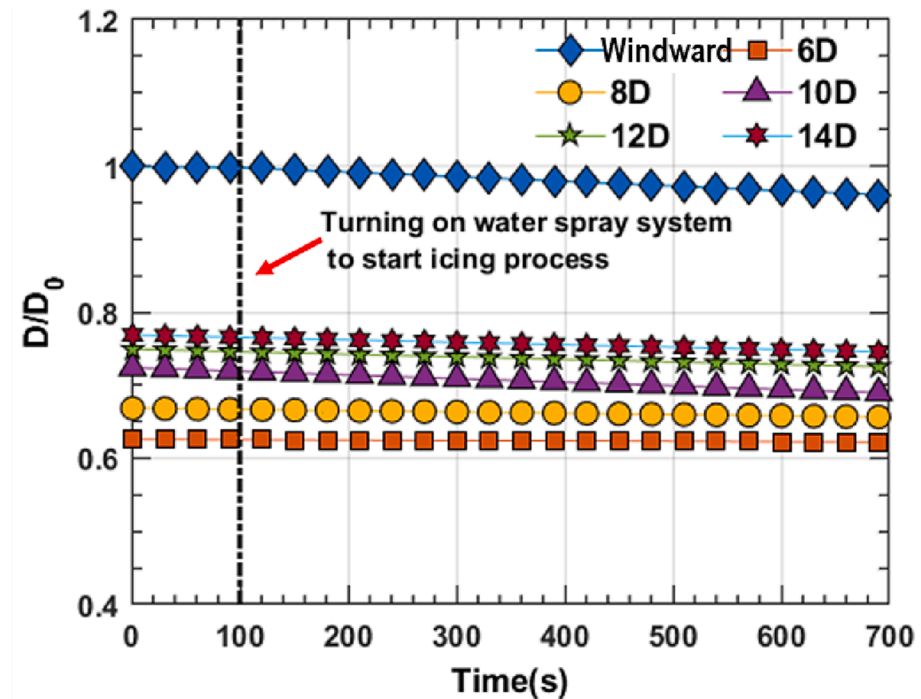

Fig. 8. Time evolution of the aerodynamic drag forces of the iced conductors for the test cases with different spacing between the bundled conductors.

smaller than that acting on the windward conductor, its magnitude varied substantially, depending on the spacing between the bundled conductors. As the spacing between the bundled conductor increases, the aerodynamic drag experienced by the leeward conductor was found to increase monotonically. While the aerodynamic drag acting on the leeward conductor was about 62% of that acting on the windward conductor for the test case with L/D = 6, the corresponding value was increased to about 78% as the spacing among the bundled conductors increased to L/D = 14.

It can also be seen that, due to the stronger "shadowing effect" from the windward conductor for the test cases with smaller spacing between

the bundled conductors, less airborne supercooled water droplets would be able to impinge onto the leeward conductor to cause less ice accretion on the leeward conductor, resulting in less outer profile changes for the iced leeward conductor. Therefore, no obvious changes were observed for the aerodynamic drag of the leeward conductor during the rime icing process for the test cases with relatively smaller spacing between the bundled conductors (i.e., less than 2%). More noticeable aerodynamic drag reduction due to the ice accretion on the leeward conductor was observed as the spacing between the bundled conductors was increased to L/D > 10, i.e., the aerodynamic drag was found to reduce about 5.0% after 600 s of the icing experiment for the test case with L/D = 14.

The present study also used a digital PIV system to characterize the wake flow behind the bundled conductors during the dynamic ice accretion process. Fig. 9 gives the PIV measurement results for three selected test cases for comparison, which include the wake flow behind the "clean" windward conductor as the comparison baseline, the wake flows behind the iced windward conductor, and the wake flows around the leeward conductors for the test cases of L/D = 6 and L/D = 12. It should be noted that while the instantaneous PIV measurements were conducted at a frequency of 15 Hz, the PIV measurement results for the iced bundled conductors given in Fig. 6 represent the ensemble-averaged PIV measurement results obtained at the last 20 s of the rime icing experiments. Simplified ice shapes accreted on the frontal surface of the conductors are also given in the graph for illustration. As revealed clearly from the PIV measurement results given in Fig. 9(a), the wake flow behind the "clean" windward conductor was featured by the presence of a relatively wide and long recirculation zone (i.e., the region with negative streamwise velocity) extending up to X/D ≈ 2.0. The wake of the windward conductor was found to expand gradually as the downstream distance increased, and the wake expanding angle was estimated to be $\theta_{wake} \approx 12°$.

As shown clearly in Fig. 9(b), after undergoing 600 s of the rime icing experiment, since the iced windward conductor was found to become more streamlined due to the ice accretion on the frontal conductor surface, the recirculation zone behind the iced windward conductor was found to become narrower with the wake expansion angle being reduced to $\theta_{wake} \approx 10°$. The narrower wake behind the iced windward conductor would indicate a smaller momentum deficit, thereby, a smaller aerodynamic drag acting on the iced windward conductor than that on "clean" windward conductor, as revealed quantitatively from the measurement data given in Fig. 8.

As revealed in Fig. 9(c), due to obvious velocity deficits behind the windward conductor, airflow speed approaching the leeward conductor was found to become much smaller than the freestream velocity,

resulting in a much smaller aerodynamic drag acting on the leeward conductor. Meanwhile, the recirculation zone behind the leeward conductor was also found to become much narrower and shorter (i.e., ending at X/D ≈ 1.5 for the L/D = 6 case). As the bundle spacing increases, the velocity deficits in the wake behind the windward conductor (i.e, the region ahead of the leeward conductor) would recover gradually. As shown in Fig. 9(d), while the incoming airflow velocity approaching the leeward conductor was found to become much greater for the test case with L/D = 12, the recirculation zone behind the leeward conductor became wider and longer (i.e., extending to X/D ≈ 2.5), in comparison to those of the L/D = 6.0 case, implying a greater aerodynamic drag acting on the leeward conductor, as confirmed by the measured aerodynamic force data given in Fig. 8.

3.2. The influences of the angular displacements among the bundled conductors

As shown schematically in Fig. 2, the effects of the angular displacement between the bundled conductors with respect to the incoming airflow were also examined in the present study. During the experiments, while the spacing between the windward and leeward conductors was fixed at L/D = 12, the bundled conductors' orientation angle (OA) about the incoming airflow was changed from 0° to 15° with an increment of 2.5°. While time sequences of the ice accretion images were acquired during the dynamic ice accretion process, Fig. 10 gives the typical snapshot images acquired after undergoing 600 s of the rime icing process. It was visualized clearly that the ice layer accreted on the leeward conductor was found to become thicker and thicker as the OA increased. By using the same image processing procedure as that used to extract the quantitative information given in Fig. 4, the time evolution of averaged thickness of the ice layer accreted near the leading edge of the leeward conductor was also determined based on the acquired ice accretion images with different OA values, and the measurement results
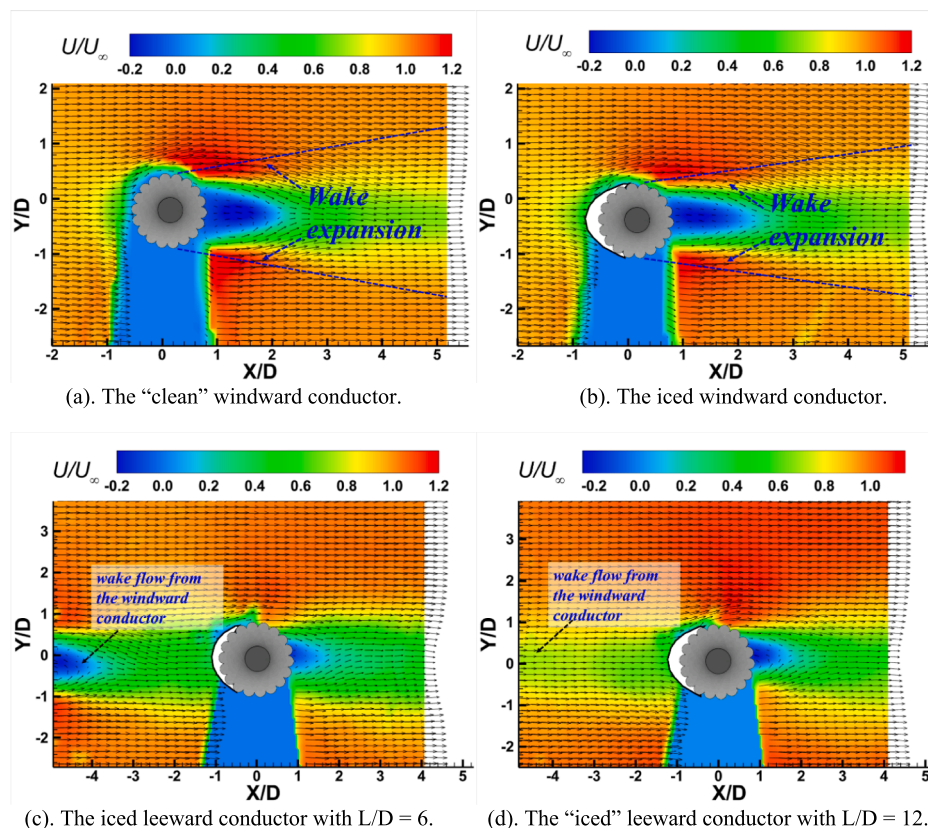

(a). The "clean" windward conductor.

(b). The iced windward conductor.

(c). The iced leeward conductor with L/D = 6.

(d). The "iced" leeward conductor with L/D = 12.

Fig. 9. Typical PIV measurement results to quantify the wake flow around the bundled conductors.
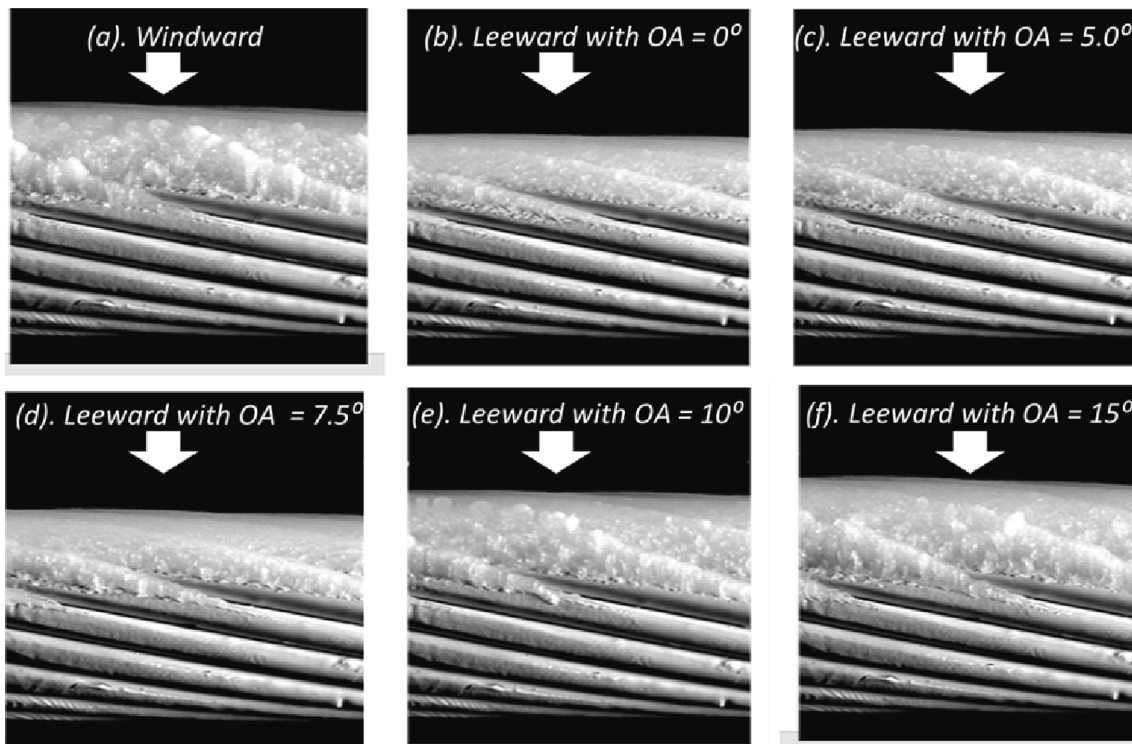
Fig. 10. Typical ice accretion images of the iced bundled conductors for the test cases with different orientation angles (OA) of the incoming airflow.

are presented in Fig. 11.

While the ice thickness on the leeward conductor increased linearly as the ice accretion time progressed for all the test cases, the accreted ice layer thickness was found to increase monotonically with the OA value of the bundled conductor until reaching $OA = 15°$. This can be explained by the fact that, as the OA values increase, the leeward conductor would be farther away from the center of the wake flow of the windward conductor, resulting in a weaker and weaker "shadowing effect" of the windward conductor on the leeward conductor. As a result, more and more airborne water droplets would be able to impinge onto the leeward conductor, causing a thicker and thicker ice layer to accrete on the leeward conductor. Based on the PIV results shown in Fig. 9, the wake expanding angle behind the windward conductor was estimated to be $θ_{wake} \approx 12°$. Therefore, the leeward conductor would be positioned out the windward conductor wake for the test case with OA = 15°, and the "shadowing effect" of the windward conductor on the leeward conductor would be almost diminished completely. Since the windward

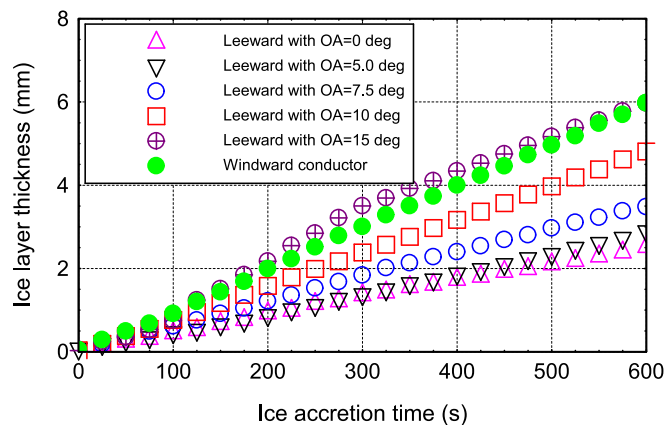and leeward conductors were exposed to the same amount of airborne water droplets, the thickness of the ice layer accreted on the leeward conductor was almost the same as that on the windward conductor for the test case with OA = 15°.

Fig. 12 shows the 3D shapes of the iced leeward conductor for the test case with L/D = 12 and OA = 7.5°. In the comparison to the test case with the leeward conductor at the center of the wake flow of the windward conductor given in Fig. 7 (i.e., the test case with L/D = 12 and OA = 0°), the ice layer accreted on the frontal surface of the leeward conductor was found to increase substantially, due to the less severe "shadowing effect" with OA = 7.5°. While the averaged outer profile of the iced leeward conductor was still found to be elliptical, the averaged ice thickness near the conductor's leading edge was estimated to be 3.81 mm, which was also found to agree well with the independently measured ice layer thickness given in Fig. 11.

Fig. 13 gives the measured aerodynamic drag of the leeward conductor positioned at L/D = 12 with the orientation angle of the bundled conductors changing from OA = 0° to OA = 15°. It was confirmed again that the aerodynamic drag acting on the leeward conductor would decrease gradually due to the continuous change in the outer profile of the iced leeward conductor (i.e., changing gradually from the bluff body to becoming more streamlined). It should also be noted that, as the OA value increases, the leeward conductor would be moved away from the wake center of the windward conductor, causing a higher airflow velocity approaching the leeward conductor. This is due to the faster recovery of the velocity deficits at the outer boundary of the wake flow. Therefore, the aerodynamic drag experienced by the leeward conductor would increase monotonically with the OA value, as shown quantitatively in Fig. 13. It is also worth noting that, while the aerodynamic drag of the leeward conductor for the test case with OA = 15° was found to be slightly smaller than that acting on the windward conductor before starting the icing experiment (i.e., ~2% smaller), however, the difference in the aerodynamic drag was found to become smaller and smaller, even being almost indistinguishable at later stages of the icing experiment (i.e., after undergoing 400 s of rime ice accretion). This can be explained by the fact that, since the windward
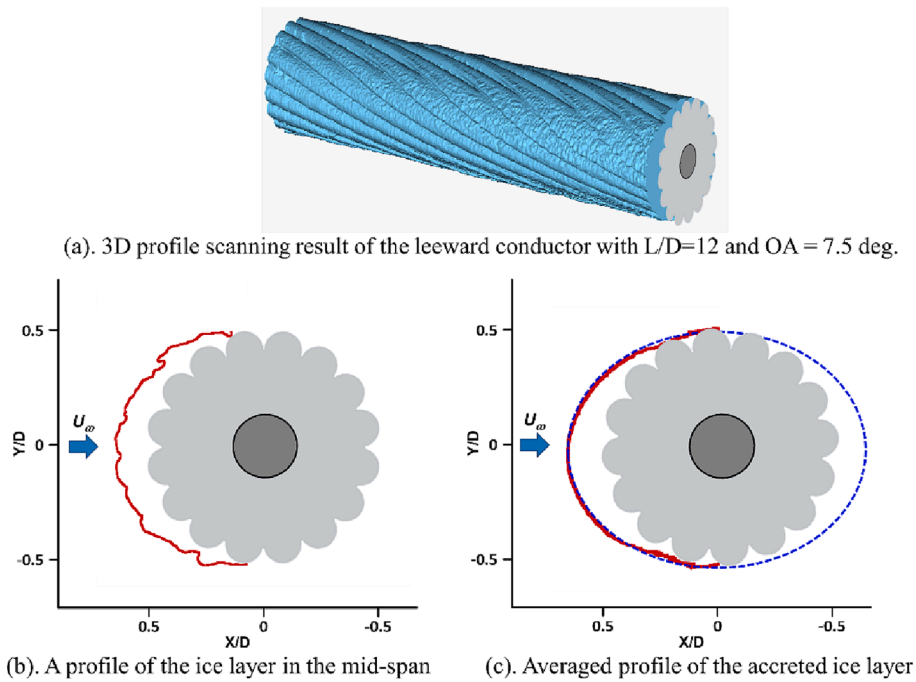

Fig. 11. The time evolution of the ice thickness on the bundled conductors with different angular displacements.

(a). 3D profile scanning result of the leeward conductor with L/D=12 and OA = 7.5 deg.

(b). A profile of the ice layer in the mid-span

(c). Averaged profile of the accreted ice layer

Fig. 12. 3D scanning results of the iced leeward conductor for the test case with L/D = 12 and OA = 7.5°.
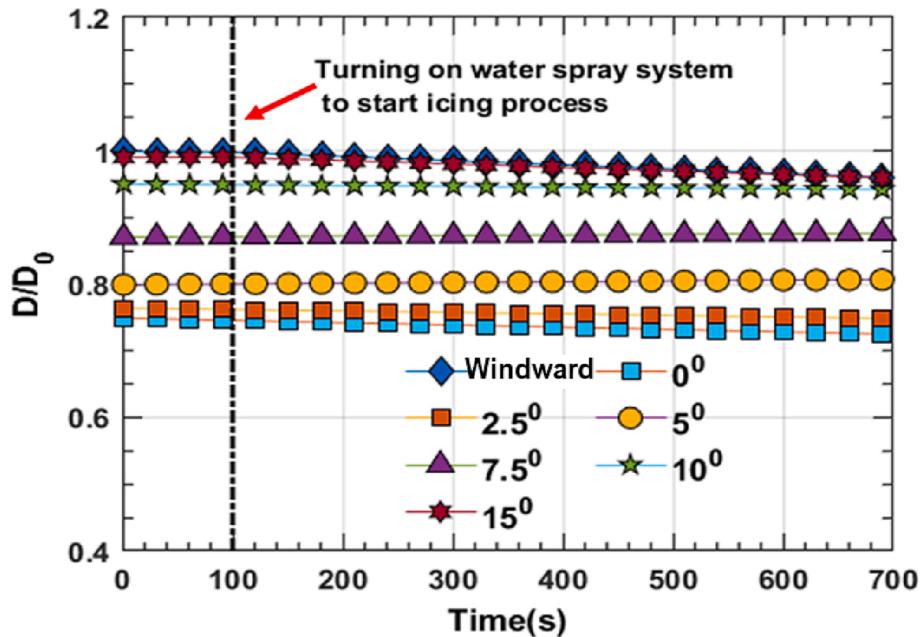

Fig. 13. The measured aerodynamic drag acting on the bundled conductors with different angular displacements.

conductor has a bluff body shape in the cross-section at the beginning of the icing experiment, the wake flow behind the windward conductor was found to expand with an averaged expanding angle of $\theta_{wake} \approx 12°$ as revealed in Fig. 9(a). As a result, even for the test case with OA = 15°, the leeward conductor may still be affected by the wake of the windward conductor from time to time, causing the slightly smaller aerodynamic drag acting on the leeward conductor at the beginning of the icing experiment (i.e., ~2% smaller than that of the windward conductor). However, with the ice layer accreted on the windward conductor becoming thicker and thicker, the outer profile of the iced windward conductor would change from a bluff body gradually to becoming more streamlined as revealed in Fig. 5, causing the wake flow behind the iced

windward conductor becoming narrower with a smaller wake expansion angle (i.e., $\theta_{wake} \approx 10°$) as revealed from the PIV measurement results given in Fig. 9(b). As a result, the leeward conductor would be positioned out of the wake of the iced windward conductor completely. Therefore, the difference in the aerodynamic drag on the windward and leeward conductors was much smaller, becoming almost indistinguishable after 400 s of the icing experiment.

4. Conclusion

An experimental study was conducted to examine the characteristics of rime ice accretion and icing-induced effects on the aerodynamic

forces acting on bundled high-voltage power conductors. While ISU Icing Research Tunnel (i.e., ISU-IRT) was used to generate a typical atmospheric rime icing condition, two pieces of Aluminum-Conductor-Steel-Reinforced (ACSR) cables were mounted in ISU-IRT with different spacing and angular displacements with respect to the incoming airflow. The rime ice layers accreted on the bundled conductors were found to be featured by the formation of well-organized ice humps, resembling the twisted outer strands of the ACSR conductors. Due to the ice accretion over the frontal conductor surfaces, the iced conductors were found to change gradually from bluff bodies to becoming streamlined in shapes. The averaged outer profiles of the iced conductors were found to be elliptical with the semi-minor axis being the radius of the ACSR conductor and the semi-major axis passing through the foremost frontal points of the accreted ice layers. As a result, the aerodynamic drag forces of the iced conductors were found to decrease gradually as the ice accretion progressed. The windward conductor was found to induce a "shadowing effect" to the leeward conductor by intercepting the supercooled water droplets carried by the incoming airflow, resulting in less ice accretion on the leeward conductor. More specifically, while the ice thickness on the leeward conductor at $L/D = 6$ was only 35% of that on the windward conductor, the corresponding value became 46% with the leeward conductor being positioned at 12D downstream from the windward conductor.

The orientation angle of the bundled conductors with respect to the incoming airflow (i.e., angular displacement) was also found to affect both the characteristics of the ice accretion and the aerodynamic force acting on the leeward conductor substantially. The "shadowing effect" of the windward conductor on the leeward conductor became weaker and weaker with the increasing orientation angle, causing both the accreted ice layer thickness and the aerodynamic drag acting on the leeward conductor to increase monotonically. As the orientation angle became larger than $15°$, the "shadowing effect" of the windward conductor on the leeward conductor diminished completely, resulting in almost identical ice accretion and aerodynamic drag characteristics of the leeward conductor to those of the windward conductor.

Declaration of Competing Interest

The authors declare that they have no known competing financial interests or personal relationships that could have appeared to influence the work reported in this paper.

Data availability

Data will be made available on request.

Acknowledgments

References

[1] N.D. Mulherin, Atmospheric icing and communication tower failure in the United States, Cold Reg. Sci. Technol. 27 (1998) 91–104, https://doi.org/10.1016/S0165-232X(97)00025-6.

[2] S. Gupta, T.J. Wipf, F. Fanous, M. Baenziger, Y.H. Hahm, Structural failure analysis of 345 kV transmission line, IEEE Trans. Power Delivery 9 (1994) 894–903, https://doi.org/10.1109/61.296272.

[3] O.F. Kv, T. Line, T.J. Wipf, D. Moines, Analysis of 345 kv transmission line, IEEE Trans. Power Delivery 9 (1994).

[4] J.C. Pohlman, P. Landers, Present state of the art of transmission line icing, IEEE Trans. Power Syst. PAS-1 (1982) 2443–2450.

[5] M. Farzaneh, Ice accretions on high-voltage conductors and insulators and related phenomena, Philos. Trans. R. Soc. A Math. Phys. Eng. Sci. 358 (2000) 2971–3005, https://doi.org/10.1098/rsta.2000.0692.

[6] X. Jiang, M. Zhu, L. Dong, Q. Hu, Z. Zhang, J. Hu, Site experimental study on suspension-tension arrangement for preventing transmission lines from icing

[7] Z. Zhang, H. Zhang, S. Yue, W. Zeng, A Review of Icing and Anti-Icing Technology for Transmission Lines, Energies (Basel). 16 (2023), https://doi.org/10.3390/en16020601.

[8] Y. Liu, H. Hu, An experimental investigation on the unsteady heat transfer process over an ice accreting airfoil surface, Int. J. Heat Mass Transf. 122 (2018) 707–718, https://doi.org/10.1016/j.ijheatmasstransfer.2018.02.023.

[9] R. Veerakumar, L. Gao, Y. Liu, H. Hu, Dynamic ice accretion process and its effects on the aerodynamic drag characteristics of a power transmission cable model, Cold Reg. Sci. Technol. 169 (2020), 102908, https://doi.org/10.1016/j.coldregions.2019.102908.

[10] M. Papadakis, A. Rachman, S. Wong, H. Yeong, C.S. Bidwell, Water Droplet Impingement on Simulated Glaze, Mixed , and Rime Ice Accretions, Nasa/Tm-2007-213961. (2007).

[11] X.-M. Li, X.-C. Nie, Y.-K. Zhu, Y. You, Z.-T. Yan, Wind Tunnel Tests on Aerodynamic Characteristics of Ice-Coated 4-Bundled Conductors, Math. Probl. Eng. 2017 (2017), https://doi.org/10.1155/2017/1628173.

[12] L. Makkonen, Modeling power line icing in freezing precipitation, Atmos. Res. 46 (1998) 131–142, https://doi.org/10.1016/S0169-8095(97)00056-2.

[13] J.L. Laforte, M.A. Allaire, J. Laflamme, State-of-the-art on power line de-icing, Atmos. Res. 46 (1998) 143–158, https://doi.org/10.1016/S0169-8095(97)00057-4.

[14] M.S. Virk, Atmospheric icing of transmission line circular conductor bundles in triplex configuration, in 2016 IEEE International Conference on Power and Renewable Energy (ICPRE), IEEE, 2016: pp. 24–28. https://doi.org/10.1109/ICPRE.2016.7871122.

[15] T. Wagner, Atmospheric Icing of Transmission Line Conductor Bundles, Proceedings of the COMSOL Conference 2008 Hannover. (2008).

[16] C.-Z. Qu, Y.-J. Liu, De-icing Method for Coupled Transmission Tower-Line System, Energy Procedia 17 (2012) 1383–1389, https://doi.org/10.1016/j.egypro.2012.02.256.

[17] R. Veerakumar, L. Tian, H. Hu, Y. Liu, H. Hu, An experimental study of dynamic icing process on an Aluminum-Conductor-Steel-Reinforced power cable with twisted outer strands, Exp. Therm Fluid Sci. 142 (2023), 110823, https://doi.org/10.1016/J.EXPTHERMFLUSCI.2022.110823.

[18] Q. He, J. Zhang, M. Deng, D. Du, M. Lasse, T. Mikko, Rime icing on bundled conductors, Cold Reg. Sci. Technol. 158 (2019) 230–236, https://doi.org/10.1016/j.coldregions.2018.08.027.

[19] L. Zhou, B. Yan, L. Zhang, S. Zhou, Study on galloping behavior of iced eight bundle conductor transmission lines, J. Sound Vib. 362 (2016) 85–110, https://doi.org/10.1016/J.JSV.2015.09.046.

[20] X. Jiang, Q. Wang, Z. Zhang, Y. Hu, Y. Pan, C. Zhu, Study on Icing Characteristics of Bundle Conductors Based on Xuefeng Mountain Natural Icing Station, in 16th International Workshop on Atmospheric Icing of Structure, 2015: pp. 2–6. https://windren.se/IWAIS_p/IWAIS2015/IWAIS2015_pa/67_03_03_Paper_Xingliang_Jiang_et_al_Study_on_Icing_Characteristics_of_Bundle_Conductors_Based_on_Xuefeng_Mountain_Natural_Icing_Test_Base.pdf (accessed February 11, 2023).

[21] F. Xu, H. Yu, M. Zhang, Y. Han, Experimental study on aerodynamic characteristics of a large-diameter ice-accreted cylinder without icicles, J. Wind Eng. Ind. Aerodyn. 208 (2021), 104453, https://doi.org/10.1016/J.JWEIA.2020.104453.

[22] J.; Liang, M.; Cai, Q.; Wang, L.; Zhou, J.; Liu, G.; Min, H. Huang, T. Stathopoulos, J. Liang, M. Cai, Q. Wang, L. Zhou, J. Liu, G. Min, H. Huang, Aerodynamic Characteristics Analysis of Iced Conductor Based on BP Neural Network, Buildings 2023, Vol. 13, Page 64. 13 (2022) 64. https://doi.org/10.3390/BUILDINGS13010064.

[23] W. Zhou, Y. Liu, H. Hu, H. Hu, X. Meng, Utilization of thermal effect induced by plasma generation for aircraft icing mitigation, AIAA J. 56 (2018) 1097–1104, https://doi.org/10.2514/1.J056358/ASSET/IMAGES/LARGE/FIGURE7.JPEG.

[24] Y. Liu, C. Kolbakir, H. Hu, X. Meng, H. Hu, An experimental study on the thermal effects of duty-cycled plasma actuation pertinent to aircraft icing mitigation, Int. J. Heat Mass Transf. 136 (2019) 864–876, https://doi.org/10.1016/j.ijheatmasstransfer.2019.03.068.

[25] L. Li, Y. Liu, H. Hu, An experimental study on dynamic ice accretion process over the surfaces of rotating aero-engine spinners, Exp. Therm Fluid Sci. 109 (2019), 109879, https://doi.org/10.1016/J.EXPTHERMFLUSCI.2019.109879.

[26] L. Tian, L. Li, H. Hu, H. Hu, Experimental Study of Dynamic Ice Accretion Process over Rotating Aeroengine Fan Blades, J. Thermophys. Heat Trans. (2022) 1–12, https://doi.org/10.2514/1.T6667.

[27] Y. Liu, W. Chen, Y. Peng, H. Hu, An experimental study on the dynamic ice accretion processes on bridge cables with different surface modifications, J. Wind Eng. Ind. Aerodyn. 190 (2019) 218–229, https://doi.org/10.1016/j.jweia.2019.05.007.

[28] Y. Peng, R. Veerakumar, Y. Liu, X. He, H. Hu, An experimental study on dynamic ice accretion and its effects on the aerodynamic characteristics of stay cables with and without helical fillets, J. Wind Eng. Ind. Aerodyn. 205 (2020), 104326, https://doi.org/10.1016/j.jweia.2020.104326.

[29] Y. Peng, R. Veerakumar, Z. Zhang, H. Hu, Y. Liu, X. He, H. Hu, an experimental study on mitigating dynamic ice accretion process on bridge cables with a superhydrophobic coating, Exp. Therm Fluid Sci. 132 (2022), 110573, https://doi.org/10.1016/J.EXPTHERMFLUSCI.2021.110573.

[30] L. Gao, H. Hu, Wind turbine icing characteristics and icing-induced power losses to utility-scale wind turbines, Proc. Natl. Acad. Sci. 118 (2021) 2111461118. https://doi.org/10.1073/PNAS.2111461118.

[31] L. Ma, Z. Zhang, L. Gao, Y. Liu, H. Hu, An exploratory study on using Slippery-Liquid-Infused-Porous-Surface (SLIPS) for wind turbine icing mitigation, Renew. Energy 162 (2020), https://doi.org/10.1016/j.renene.2020.10.013.

[32] L. Gao, Y. Liu, H. Hu, An experimental investigation of dynamic ice accretion process on a wind turbine airfoil model considering various icing conditions, Int. J. Heat Mass Transf. 133 (2019) 930–939, https://doi.org/10.1016/J.IJHEATMASSTRANSFER.2018.12.181.

[33] L. Gao, Y. Liu, L. Ma, H. Hu, A hybrid strategy combining minimized leading-edge electric-heating and superhydro-/ice-phobic surface coating for wind turbine icing mitigation, Renew. Energy 140 (2019) 943–956, https://doi.org/10.1016/J.RENENE.2019.03.112.

[34] J. Li, B. Du, J. Su, H. Liang, Y. Liu, Surface Layer Fluorination-Modulated Space Charge Behaviors in HVDC Cable Accessory, Polymers (Basel). 10 (2018) 500, https://doi.org/10.3390/polym10050500.

[35] D.N. Anderson, J.C. Tsao, Overview of icing physics relevant to scaling, SAE Technical Papers (2003), https://doi.org/10.4271/2003-01-2130.

[36] K. Zhang, T. Wei, H. Hu, An experimental investigation on the surface water transport process over an airfoil by using a digital image projection technique, Exp. Fluids 56 (2015) 1–16, https://doi.org/10.1007/s00348-015-2046-z.

[37] L. Gao, R. Veerakumar, Y. Liu, H. Hu, Quantification of the 3D shapes of the ice structures accreted on a wind turbine airfoil model, J. Vis. (Tokyo). 22 (2019) 661–667, https://doi.org/10.1007/s12650-019-00567-4.

[38] Z. Zhang, Y. Liu, H. Hu, Effects of chamber pressure on the kinematic characteristics of spray flows exhausted from an airblast atomizer, Exp. Therm. Fluid Sci. 130 (2022), 110514, https://doi.org/10.1016/j.expthermflusci.2021.110514.

[39] R.J. Hansman, M.S. Kirby, Comparison of wet and dry growth in artificial and flight icing conditions, J. Thermophys. Heat Trans. 1 (1987) 215–221, https://doi.org/10.2514/3.30.

[40] Y. Liu, L. Li, H. Li, H. Hu, An experimental study of surface wettability effects on dynamic ice accretion process over an UAS propeller model, Aerosp. Sci. Technol. 73 (2018) 164–172, https://doi.org/10.1016/j.ast.2017.12.003.

[41] L. Gao, T. Tao, Y. Liu, H. Hu, A field study of ice accretion and its effects on the power production of utility-scale wind turbines, Renew. Energy 167 (2021) 917–928, https://doi.org/10.1016/j.renene.2020.12.014.

[42] Y. Liu, L.J. Bond, H. Hu, Ultrasonic-Attenuation-Based Technique for Ice Characterization Pertinent to Aircraft Icing Phenomena, AIAA J. (2017) 1–8, https://doi.org/10.2514/1.J055500.

[43] L. Qi, M. Wang, G. Xu, Z. Wang, Numerical Simulation of Aerodynamic Forces of ACSR Conductor, Proceedings of the 2015 International Conference on Applied Science and Engineering Innovation. 12 (2015). https://doi.org/10.2991/ASEI-15.2015.375.